Cell Reports
Physical Science

CellPress
OPEN ACCESS

Article

Engineering bimetallic interfaces and revealing the mechanism for carbon dioxide electroreduction to C_{3+} liquid chemicals

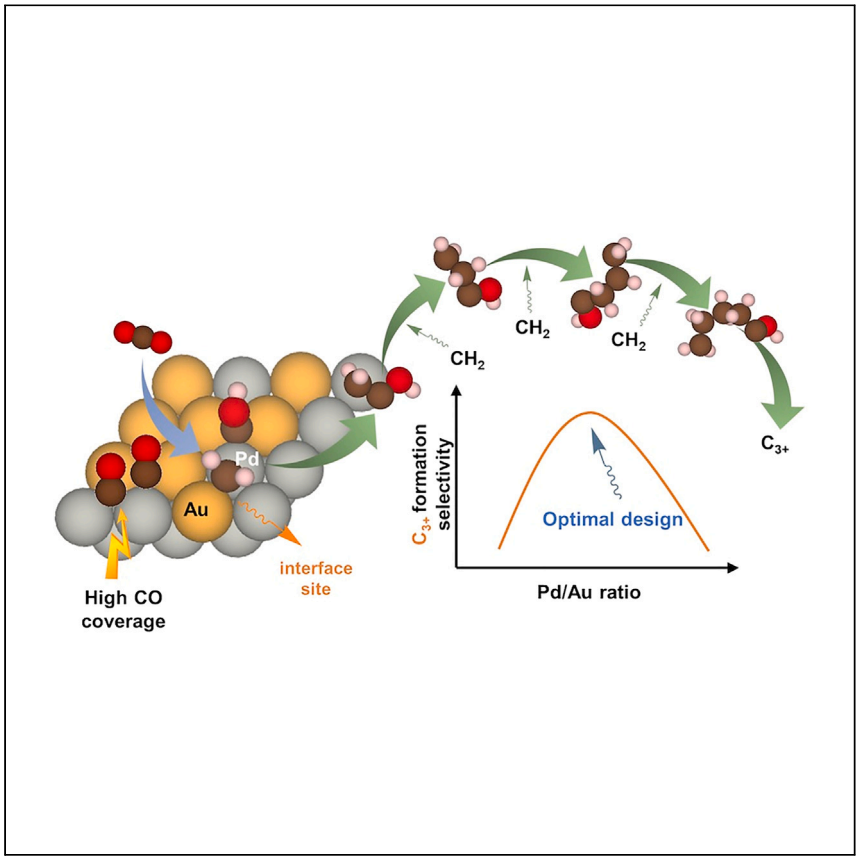

Xu et al. investigate carbon dioxide electroreduction to C_{3+} products over bimetallic interfaces. They identify key intermediates and rate-limiting steps, ultimately indicating how tuning the bimetallic interface and surface coverage can lead to optimized C_{3+} chemical generation.

Yuting Xu, Michael B. Ross, Hongliang Xin, Fanglin Che

fanglin_che@uml.edu

Highlights

CO_2 reduction to C_{3+} products over bimetallic systems is performed theoretically

CH_2–C_1 coupling is identified as the potential rate-limiting step

Tuning the carbon monoxide coverage can promote C_{3+} product generation

Optimizing the palladium/gold surface ratio can lower the activation barrier for C–C coupling

Xu et al., Cell Reports Physical Science 4, 101718
December 20, 2023
https://doi.org/10.1016/j.xcrp.2023.101718

Cell Reports
Physical Science

CellPress
OPEN ACCESS

Article

Engineering bimetallic interfaces and revealing the mechanism for carbon dioxide electroreduction to C_{3+} liquid chemicals

Yuting Xu,[1] Michael B. Ross,[2] Hongliang Xin,[3] and Fanglin Che[1,4,*]

SUMMARY

The reduction reaction of carbon dioxide (CO_2RR) to liquid C_{3+} chemicals is a potential net-zero carbon process that can increase local resiliency to power outages and fuel consumption. However, the mechanism and catalyst design rules to promote CO_2RR-to-C_{3+} are unknown. Engineering bimetallic interfaces (e.g., palladium/gold) to tune intermediate adsorption is promising for promoting C_{3+} formation. Our density functional theory calculations find that $*CH_2$ could be the key intermediate, and C_1–CH_2 coupling could be the rate-limiting step to generate C_{3+}. High CO surface coverages can promote the bimetallic interfacial sites, lower the energetics of the C_1–CH_2 coupling step, and enhance C_{3+} formation. We further construct a volcano plot of C_1–CH_2 kinetics as a function of the binding strength of key intermediate $*CH_2$ via engineering the *d*-band center of the interfacial site. Our findings could guide the rational design of bimetallic interfaces and their near-surface microenvironment for enhancing CO_2RR-to-C_{3+}.

INTRODUCTION

With environmental concerns of greenhouse gas emissions (e.g., CO_2) and the urgent needs to reduce energy reliance on fossil fuels, there is a growing interest in finding a clean and sustainable way to capture and utilize CO_2 to produce high-value chemicals.[1] CO_2 to C_{3+} chemicals has potential in energy and chemical sectors.[2,3] C_{3+} chemicals act as important energy carriers, offering sustainable and efficient power. They serve as vital feedstocks for industries like automotive, construction, packaging, and textiles.[4,5] Moreover, they can be converted into valuable chemicals (alcohols, aldehydes, and ketones) used in pharmaceuticals, cosmetics, agriculture, and specialty chemicals.[6–9] Electrocatalytic CO_2 reduction reaction (CO_2RR), utilizing renewable electricity, has emerged as a promising approach for converting CO_2 into C_{3+} products.[10,11] Electrocatalysis offers distinct advantages, including protons from water, precise control over reaction conditions, adjustable selectivity, the potential for integration with renewable energy sources, and portable, modular setup.[3,12] Ongoing research and development endeavors are focused on designing novel electrocatalysts, controlling the microenvironment near the electrodes, and optimizing the electrocatalytic device to enhance energy efficiency and to advance the commercial viability of electrocatalytic CO_2 conversion into C_{3+} products.[13–16]

For the C_{3+} products from CO_2RR, Zhou et al.[17] utilized inorganic nickel oxygenate-derived electrocatalysts to generate C_{3+} products through CO_2RR. They stated that the Fischer-Tropsch-like mechanism, where CH_x–CO species were converted into C_2 species and, subsequently, higher hydrocarbons were synthesized through CH_x

[1]Department of Chemical Engineering, University of Massachusetts Lowell, Lowell, MA 01854, USA

[2]Department of Chemistry, University of Massachusetts Lowell, Lowell, MA 01854, USA

[3]Department of Chemical Engineering, Virginia Polytechnic Institute and State University, Blacksburg, VA 24061, USA

[4]Lead contact

*Correspondence: fanglin_che@uml.edu

https://doi.org/10.1016/j.xcrp.2023.101718

insertion, could be the mechanism of CO_2RR to C_{3+}. Maeng et al. experimentally observed the presence of C_2–C_5 hydrocarbons on a Pt/Cd electrode.[18] They reported that these hydrocarbons followed the Anderson-Schulz-Flory distribution, indicating that surface polymerization reactions followed the Fischer-Tropsch mechanism and contributed to the formation of long-chain hydrocarbons.[18]

Regarding the theoretical mechanism studies on generating C_{3+} during CO_2RR, one key step of generating C_{3+} product could be via C_1–C_2 coupling and thus, it is essential to form C_2 from CO_2.[19,20] Previous theoretical and experimental studies have identified CO (or COH/CHO) as the key intermediate species and CO dimerization as the key elementary step for C_2 product formation.[21–23] Zhou et al.[24] and Xiao et al.[25] reported that a large difference of the binding energies of two CO species could promote the CO dimerization toward C_2 products during CO_2RR. Therefore, a design rule for CO_2RR-to-C_{3+} is to have one component, such as gold (Au) and silver (Ag) to weakly bind the CO molecule and another component, such as palladium (Pd), nickel (Ni), and platinum (Pt) to strongly bind the other CO molecule.[26–31] Kortlever et al.[32] reported that Pd/Au alloys (with strong CO–Pd bond and weak CO–Au bond) can provide dual active sites to facilitate the production of C_3–C_5 products. This electrocatalyst, composed of Pd and Au, firstly represents a significant advancement as a Cu-free catalyst capable of producing a diverse range of multi-carbon (C_3–C_5) products from CO_2. By tuning the binding strength of CO via the combination of Pd and Au, this catalyst exhibits an onset potential of -0.8 V_{RHE} and demonstrates the detection of C_3–C_5 hydrocarbons. The experimental results indicate that an excess of Pd on the surface facilitates the production of C_{3+} hydrocarbons. Additionally, their investigation into the selectivity for long-chain hydrocarbon formation reveals that Pd/Au alloy systems enhance the CO_2RR process, favoring the production of C_{3+} hydrocarbons while suppressing hydrogen evolution reactions compared to Pd systems. However, very few studies investigated the detailed mechanism of CO_2RR-to-C_{3+} process, resulting in a trial-and-error approach for experimental catalysts and operation designs due to our limited understanding on the mechanism, key intermediates, and potential rate-limiting steps of this process.

Inspired by Fischer-Tropsch mechanism and previous theoretical mechanism studies,[17,33] *CO and *CH_2 can be the key intermediates for CO_2RR to long-chain hydrocarbon products via C_1-C_n coupling. We thus hypothesize that engineering the binding strength of *CO and *CH_2 over catalytic surfaces could significantly enhance the production of C_{3+} chemicals during CO_2RR. Inspired by the design rule of having alloy system with one strongly bonding to CO and one weekly bonding to CO, we chose Pd/Au alloy system as a model catalyst to study the mechanism of CO_2RR-to-C_{3+} via density functional theory (DFT) calculations.[32,34–36] We proposed possible mechanisms of CO_2RR-to-C_{3+} with *CO and *CH_2 as the key intermediates (Scheme 1).[17,19,37–39]

In this work, we first studied the energetics of the C_1–C_n coupling process via various C_1 intermediates (*CO and *CH_2) for CO_2RR-to-C_{3+}. We then determined the thermodynamic favorable mechanism of *CH_2 formation from CO_2. In particular, we investigated the effects of bimetallic interface and CO surface coverages on the energetics of C–C coupling and key intermediates formation during CO_2RR-to-C_{3+}. Furthermore, based on the *d*-band theory, we further engineered the *d*-band center of various Pd/Au bimetallic interfaces to maximize the production of C_{3+} chemicals via minimizing the energetics of C–C coupling. This work will advance the in-depth understanding of the CO_2RR-to-C_{3+} mechanism, the potential key intermediates, and rate-limiting steps. *Ab initio* DFT modeling offers exceptional possibilities to

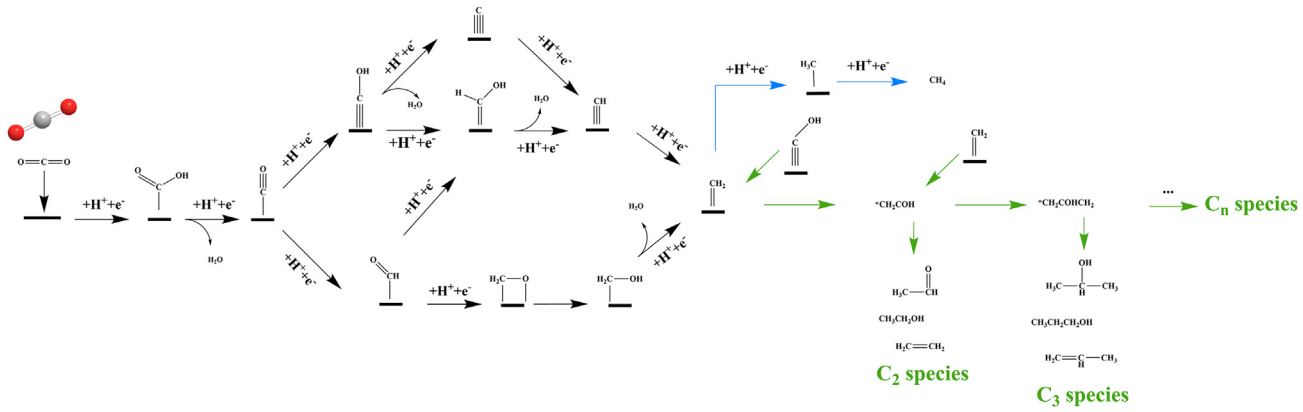

Scheme 1. The proposed mechanism

In particular, the proposed reaction mechanism for CO_2RR-to-C_{3+} via the key intermediates of *CH_2 and *CO.

facilitate catalyst development and create the opportunity to enter a new paradigm in catalyst design based on fundamentals rather than trial and error for CO_2-to-C_{3+}.

RESULTS AND DISCUSSION

Computational setup

DFT calculations were performed using the Vienna Ab-initio Simulation Package (VASP) with revised Perdew-Burke-Ernzerhof (RPBE) exchange–correlation functional.[40] The reason for choosing RPBE is that RPBE introduces an additional term to correct for the self-interaction error form PBE functional, which leads to an improved accuracy of species adsorption energetics (e.g., the key intermediate CO binding energy).[41] We simulated a Pd-rich Pd/Au bimetallic slab with three layers of Pd and a top layer of 75% Pd/Au ratio (note: the catalyst model is based on the experimental work from Kortlever et al., and we also tried various configurations at this Pd/Au ratio to obtain the most stable configuration) (see Figure S1) to investigate the mechanism of CO_2RR-to-C_{3+} processes (Figure S2A).[32,42] For comparisons, pure Pd(111) and Au(111) with four layers p(4 × 4) supercells were created (Figures S2B and S2C). The adsorbates and the top two metal layers were relaxed until the forces were smaller than 0.03 eV/Å and reached the energy accuracy of 10^{-4} eV. The Brillouin zones of all surfaces were sampled with 3 × 3 × 1 Monkhorst-Pack k-points. The kinetic energy cutoff for plane-wave basis was set as 500 eV.

Four possible pathways for CO_2RR-to-CH_2 have been proposed in this work with six proton-electron transfer elementary steps (Scheme 1). For each examined catalyst surface (Pd, Au, Pd/Au), all possible adsorption sites (Figure S3) have been tested to obtain the most favorable adsorption configurations for the mechanism-involved intermediates (Figures S4–S16 and Table S1). The Gibbs free energy diagram of CO_2RR-to-CH_2 has been established via combining DFT calculations and statistical mechanics. The Gibbs free energy of each proton-electron transfer elementary step has been calculated using the computational hydrogen electrode (CHE) model.[25] In the CHE model, the proton-electron transfer process can be referred to half H_2 ($\frac{1}{2}H_2 \leftrightarrow H^+ + e^-$). All calculations were conducted under standard conditions (e.g., 1 atm and room temperature).

Incorporating solvation and applied potential effects is also a crucial element when simulating solid-electrolyte interfaces under electrochemical conditions,[23] since

solvation and applied potentials can play a significant role in stabilizing reaction intermediates, thereby influencing the energetics of pathways and potentially acting as a mediator that impacts the activation barrier to rate-determining step (RDS).[43,44] To incorporate the solvation, we considered both the bulk water solvation using an implicit solvation model embedded in VASPsol combined with the explicit interface water molecules.[45–48] In the VASPsol model, the solvent was treated as a continuous medium, and the solvent effect was expressed using the dielectric constant. The electrolyte solution was simulated using a linearized Poisson-Boltzmann model. In this particular instance, we employed a dielectric constant (ε) of 78.4, which was the dielectric constant of water solvent.

Furthermore, we have also applied constant electrode potential (CEP) model[49] to investigate the surface charge and cation effects using grand-canonical DFT (GC-DFT) calculations. At room temperature, the Debye screening length (Å) can be calculated from the electrolyte concentration (M) with the equation as following:[50]

$$\kappa = \frac{3}{\sqrt{I}}, \quad \text{(Equation 1)}$$

where κ is the Debye length and I notes the electrolyte concentration. Thus, a Debye screening length of 9.61 Å was used to model an electrolyte concentration of 0.1 M, which follows Kortlever et al.'s experimental conditions.[32,51,52] To consider the applied potential in the CEP model, the Fermi level (E_f) with vacuum potential at 0 eV is tuned to a target value by varying the number of electrons added or removed in the system, allowing the work function (Φ) and, therefore, the electrode potential with reference to SHE (U_{SHE}) to be fixed:

$$U_{SHE} = \frac{\Phi - \Phi_{SHE}}{e}, \quad \text{(Equation 2)}$$

where Φ_{SHE} is the work function of standard hydrogen electrode and Φ_{SHE} = 4.43 eV is determined by RPBE for the thermodynamic work function of the standard hydrogen electrode (SHE).[53] By adjusting the number of additional electrons introduced into the systems, we maintain a constant potential of approximately −1.30 V vs. SHE for each reaction based on the experiments results.[51] The reaction energy of A→B under the constant applied potential can be represented as[54]:

$$\Delta H_{rxn}^{sol} = E_{DFT}(B)\text{-}E_{DFT}(A)\text{-}\mu_e(N_e(B)\text{-}N_e(A)), \quad \text{(Equation 3)}$$

where E_{DFT} is the electronic energy of the charged unit cell obtained by DFT calculations, N_e is the number of electrons in the unit cell, and μ_e is the chemical potential of the electron.

We further calculated the energetics (e.g., reaction energies and activation barriers) of the reduction reactions to methane and C–C coupling processes to C_{3+} chemicals. More computational details (e.g., how to calculate the Gibbs free energy and activation barriers, the configurations and energetics of CO_2RR-to-CH_2 intermediates and C–C coupling over various Pd/Au alloy surfaces) are given in the Supplemental information.

C_1–C_n coupling to long-chain chemicals during CO_2RR

To form long-chain liquid C_{3+} chemicals from CO_2RR, the C_1–C_n coupling steps are essential. We have calculated energetics of C_1–C_n coupling to form C_{3+} over a Pd/Au(111) surface and compared with that over the pure Pd(111) surface. According to the literature review, it should be CO dimerization (i.e., $CO + COH \leftrightarrow OCCOH$)

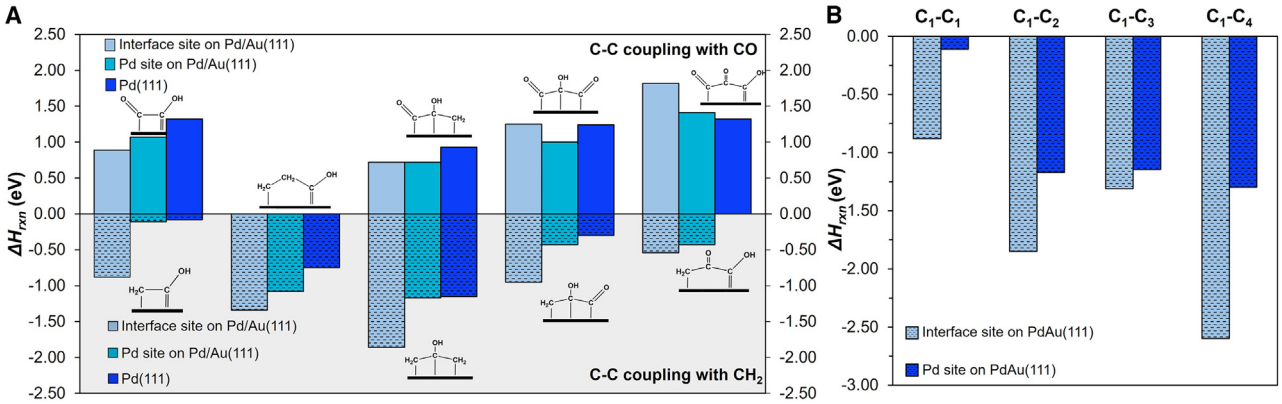

Figure 1. Reaction energetics for C-C coupling

(A) The DFT-calculated reaction energies (ΔH_{rxn}) for C_1–C_1 and C_1–C_2 coupling over Pd/Au(111) with a comparison of Pd(111). Here, we compared *CO and *CH_2 as the key C_1 intermediates. For the Pd/Au(111) surface, both Pd/Au interfacial sites and pure Pd sites were considered for the C_1 adsorption during the C_1–C_n coupling processes. The C_1–C_1 coupling processes include *CO–COH and *CH_2–COH. When CO serves as the C_1 intermediate, the C_1–C_2 coupling processes include *CO–$COHCH_2$, *CO–COHCO, and *CO–COCOH. *CO and *CH_2COH did not tend to bond with each other in DFT calculations. When *CH_2 serves as the C_1 intermediate, C_1–C_2 coupling processes include *CH_2–CH_2COH, *CH_2–$COHCH_2$, *CH_2–COHCO, and *CH_2–COCOH. For *CH_2–COCOH coupling over the Pd(111) surface, the reaction energy is around 0 Ev and, thus, it is hard to see this step from the figure. (B) The DFT-calculated reaction energies (ΔH_{rxn}) for C_1–C_n from C_1–C_1 to C_1–C_4 over Pd/Au(111) surface with interface and Pd sites for comparison (Here, C_1 is the CH_2 species). The geometries of the initial and final states of the examined C–C coupling steps were shown in Figures S17–S27.

to produce C_2 products over the Cu-based catalysts.[55] However, Cu-based catalysts have very poor selectivity to generate C_{3+}, suggesting CO dimerization might not be the mechanism for generating C_{3+} chemicals. Inspired by Fischer-Tropsch mechanism, *CH_2 could serve as the key intermediates for generating C_{3+} chemicals.[56]

With this background, we first calculated the reaction energies of C_1–C_n coupling to C_{3+} products over different sites (e.g., Pd/Au interface site, pure Pd site) of Pd/Au(111) with a comparison of the bare Pd(111) surface (Figure 1A). We also compared *CO and *CH_2 as the intermediates for C_1–C_n coupling to identify the most favorable C_1 intermediate.

Based on our DFT results, all the reaction energies for C_1–C_n coupling steps with *CO as the intermediates are positive (endothermic), while the same coupling reactions are exothermic with *CH_2 as the key intermediate. That is, *CH_2 is more promising to favor the formation of long-chain C_{3+} hydrocarbons during the CO_2RR processes. Thus, the Ficher-Trophsch-like mechanism with the polymerization of surface methylene (–CH_2) could be employed to form C_{3+} products.[56]

To produce longer carbon-chain products, C_1–C_n coupling reactions to form C_2–C_5 products have been also investigated in this study. According to the DFT results, our proposed Pd/Au systems demonstrate the ability to generate C_{3+} products, as depicted in Figure 1B. Evidently, the reactions subsequent to C_1–C_1 become progressively easier, accompanied by a substantial reduction in reaction energies. Thus, the C_1–C_1 step should be the potential RDS during the C_1–C_n coupling processes, since they have much higher reaction energies than those of the C_1–C_{2+} coupling steps (Figure 1). We further calculated the activation barriers (E_a) (Figure S28) for the most favorable C_1–C_1 and C_1–C_2 coupling steps. The calculated E_a of *CH_2–COH over the Pd/Au surface is 1.34 eV, which is 0.7 eV higher than that of the *CH_2–$COHCH_2$ coupling step. Taken together, *CH_2–C_1 coupling could be the potential RDS.

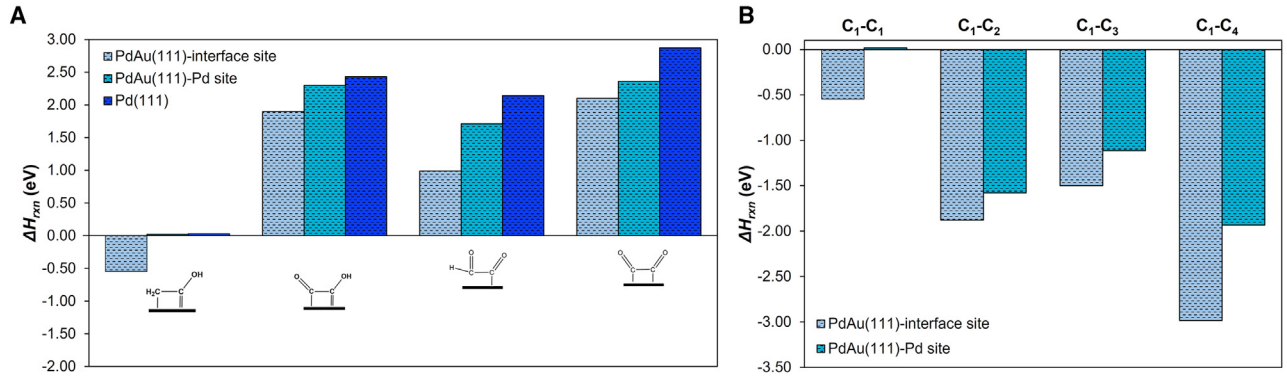

Figure 2. Hybrid solvation effects on C–C coupling

(A) With solvation effects, the DFT-calculated reaction energies (ΔH_{rxn}) for C_1–C_1 over Pd/Au(111) with a comparison of Pd(111) including COH–CH_2, CO–COH, CO–CHO, and CO–CO. For the Pd/Au(111) surface, both Pd/Au interfacial sites and pure Pd sites were considered for the C_1 adsorption during the C_1–C_1 coupling processes.

(B) With solvation effects, the DFT-calculated reaction energies (ΔH_{rxn}) for C_1–C_n from C_1–C_1 to C_1–C_4 over Pd/Au(111) surface with interface and Pd sites for comparison (here, C_1 is the CH_2 species). The geometries of the initial and final states of the examined C–C coupling steps were shown in Figures S30–S36.

In addition, the potential RDS, *CH_2–C_1 coupling is more thermodynamically favorable at the interface site of the bimetallic system than the other sites. For example, the reaction energy of *CH_2–COH coupling is −0.88 eV when the *CH_2 adsorbed at the Pd/Au interface sites (Figure S18), while the reaction energy increases to −0.11 eV when the CH_2 adsorbed at the Pd sites over Pd/Au(111). In summary, to facilitate CO_2RR-to-C_{3+}, we need to enhance the formation of the key intermediate *CH_2 and lower the energetics of the potential RDS—the CH_2–C_1 coupling step via exposing and engineering more bimetallic interfacial sites (e.g., Pd/Au).

Hybrid solvation approach and applied potential effects on the C–C coupling reactions

Focusing on C_1–C_1 coupling, which has been distinguished as the potential RDS for long carbon chain formation processes, more combinations, including CH_2–COH, CO–COH, CO–CHO, and CO–CO have been investigated with considering implicit and explicit solvation effects simultaneously. After incorporating the solvation effects, the reaction energies pertaining to C_1–C_1 coupling reactions over Pd(111) and Pd/Au(111) surfaces (both the Pd site and the Pd–Au interface site) have been calculated and presented in Figure 2. Our results show that COH–CH_2 is still the most favorable reaction for C_1–C_1 coupling with solvation effects. In addition, for C_1–C_n coupling in the presence of solvation effects, the reaction energetics are more thermodynamically favorable as increasing the carbon chain lengths (Figures 2 and S29–S35). Therefore, our conclusion remains the same that CH_2 is the key intermediate for C–C coupling reactions to form longer carbon chains and C_1–C_1 coupling is the potential RDS in the presence of solvation effects.

Furthermore, we considered the applied potential effects via CEP model using GC-DFT calculations. We applied a constant potential of −1.30 V vs. SHE to the C–C coupling reactions (Figure 3). Clearly, the C_1–C_1 coupling reaction with CH_2 as the key intermediate remains the most favorable pathway. The application of a constant potential significantly reduces the reaction energy. Among the various sites involved in the C–C coupling processes, interfacial sites exhibit a remarkable enhancement in facilitating carbon chain formation for each C–C coupling reaction. In particular, the

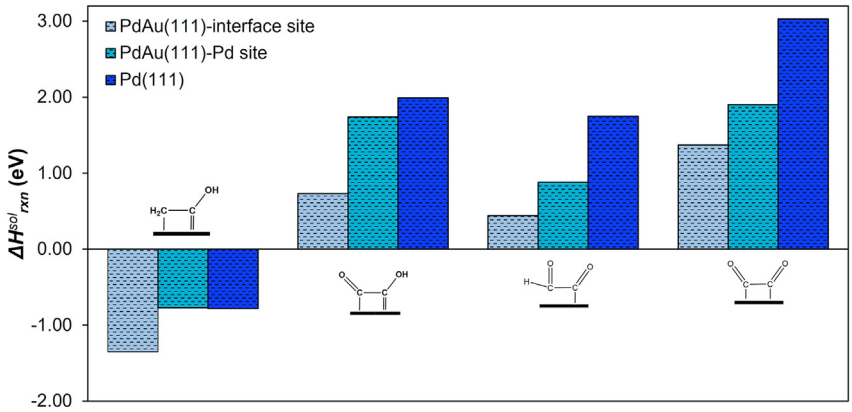

Figure 3. Applied negative potential effects on C–C coupling

The GC-DFT-calculated reaction energies with solvation effects (ΔH_{rxn}^{sol}) for C_1–C_1 over Pd/Au(111) with a comparison of Pd(111) including COH–CH_2, CO–COH, CO–CHO, and CO–CO. For the Pd/Au(111) surface, both Pd/Au interfacial sites and pure Pd sites were considered for the C_1 adsorption during the C_1–C_1 coupling processes. For all of the reactions, the applied potential is a constant of −1.30 V vs. SHE with tuning the number of extra electrons.[32] Following the experimental conditions, 0.1 M phosphate buffer electrolyte was employed in this part with Debye length of 9.61 Å.

reaction energy can be reduced from −0.55 eV to −1.35 eV when the key intermediate is located on an interfacial site in the case of COH–CH_2 coupling.

Proposed key intermediate *CH_2 formation

To favor the formation of the key intermediate *CH_2 during CO_2RR, four possible mechanisms have been proposed (Scheme 1). To identify the most thermodynamically favorable reaction pathway for the *CH_2 formation over different surfaces (e.g., Pd/Au, Pd), the Gibbs free energy diagrams have been established.[57,58] For the bare Pd(111) surface, the most thermodynamically favorable reaction pathway for CO_2RR-to-CH_2 passes the key intermediates of *CO, *CHO, and *HCOH. While the most thermodynamically favorable pathway over the Pd/Au(111) bimetallic surface passes the key intermediates of *CO, *COH, and *HCOH (Figure 4). The details about Gibbs free energy calculation have been explained in the supplemental experimental procedures (with Equations 2 and S6). For the most favorable reaction pathway for CO_2RR-to-CH_2 over pure Pd(111) and Pd/Au(111), the potential RDS is the first proton-electron transfer step of CO_2 to form *OCOH due to its highest reaction energy. The results agree well with Hossain et al.[59] and Singh et al.[60] that the RDS for CO_2RR-to-CH_2 is the first proton-electron transfer from CO_2 to *COOH. The energy requirement for this potential RDS step over the Pd/Au(111) surface is 0.34 eV, which is significantly lower than that of the Pd(111) surface (0.57 eV). Thus, one should expect that engineering the PdAu alloy system can favor the activation of CO_2 to form *CH_2 than that over the bare Pd system. As hydrogen evolution reaction (HER) can be competitive to CO_2RR, the free energy diagram for H_2 formation process has also been investigated (Figure S36) over PdAu(111) and Pd(111) surfaces. Our results show that PdAu interfacial site significantly suppressed HER compared to that over pure Pd system or over the Pd site of the PdAu alloy system.

Exposing the Pd/Au interfacial sites via tuning *CO coverages

Over the Pd/Au bimetallic surface, one should expect that the CO_2RR-related C_1 intermediate would favor to bind over the Pd sites rather than the Pd/Au interfacial sites due to the strong binding energy of C_1–Pd (Figures S4–S16). To expose the

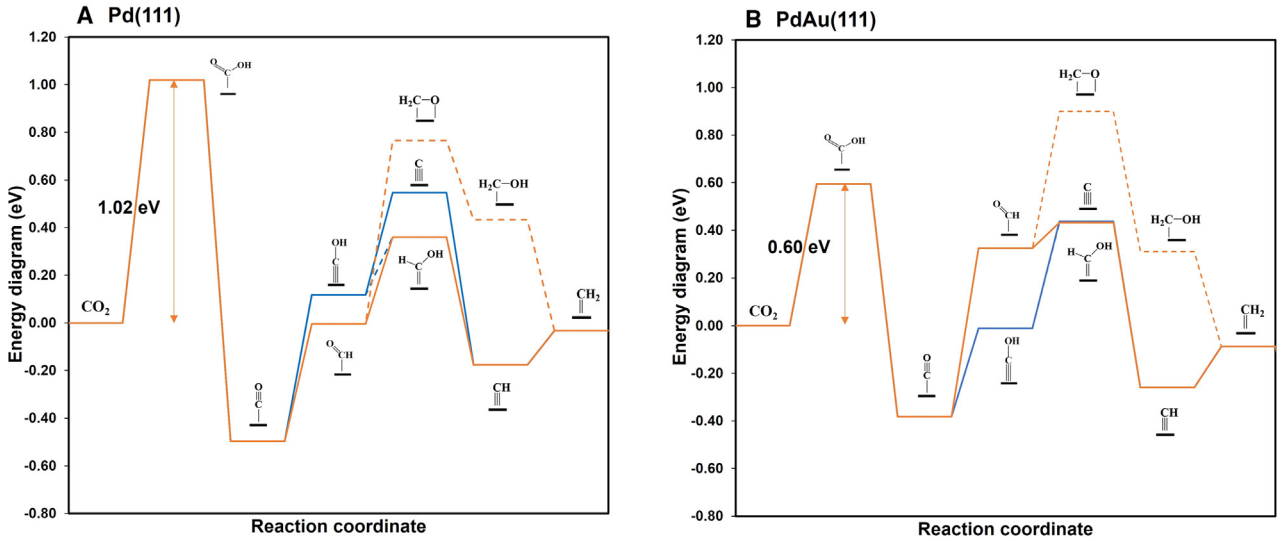

Figure 4. Gibbs free energy diagrams for CO_2RR-to-CH_2 at 0 V vs. SHE

The energy diagram of CO2RR-to-CH_2 (following the possible reaction paths in Scheme 1) over (A) a pure Pd(111) surface and (B) a bimetallic Pd/Au(111) surface.

Pd/Au interfacial sites for the *CH_2 formation, various surface coverages of the key intermediate *CO over the catalyst surface were performed. We have calculated the free adsorption energy per *CO for the most favorable *CO configuration over both Pd(111) and Pd/Au(111) surfaces at different surface coverages, ranging from 1/16 monolayer (ML) to 3/4 ML (Figures 5 and S37). To compare different Pd/Au alloy surfaces, 75%Pd/Au and 50%Pd/Au have been compared in Figure 5. At all examined *CO surface coverages, pure Pd surface presents stronger *CO binding energy than that over Pd/Au. At a lower *CO surface coverage (i.e., <1/2 ML), per *CO binding energy over Pd and Pd/Au is nearly the same when *CO prefers to adsorb over the Pd sites of Pd/Au system. When *CO surface coverage increases to 1/2 ML over the Pd/Au surface, *CO starts to occupy over the interface site (the insert picture in Figure 5). Per *CO binding energy over the Pd/Au surface is weaker than that over the bare Pd surface. As the CO coverage increased over ~11/16 ML, the free adsorption energy per *CO is close to 0 eV and thus, CO is less likely to bind over the examined surfaces. Therefore, a high surface coverage of *CO, i.e., >1/2 ML, can promote the exposure of the bimetallic interface sites. For our following mechanism studies of C_{3+} formation from CO_2, we have selected the system with 1/2 ML of *CO to investigate the surface coverage effects. Furthermore, when a 50% Pd/Au ratio is employed, it results in a *CO binding strength that is comparatively weaker than that observed on the 75% Pd/Au(111) surface. Additionally, the formation of interfacial sites on the 50% Pd/Au(111) surface is achievable at a lower CO surface coverage of 3/8 ML. This implies that reducing the Pd/Au ratio from 100% to 50% can lead to a reduction in the CO surface coverage requirement for the creation of Pd/Au interfacial sites, which, in turn, facilitates C–C coupling.

Experimentally, *CO has been detected to favorably adsorb at the atop site over the metal surfaces (e.g., Pd) rather than the hollow sites in our theoretical DFT calculations due to the an overestimation of the interaction between the vacant CO 2π* orbitals and the metallic *d*-band using RPBE functionals.[61,62] Regarding the disparity between experimental results and DFT theoretical predictions, we additionally

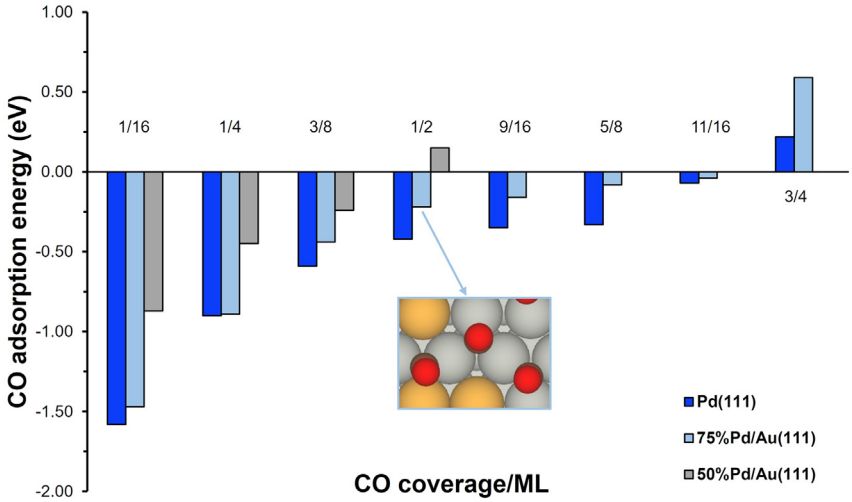

Figure 5. Free adsorption energy per CO as a function of CO coverages

For PdAu(111) surfaces, 75%Pd/Au and 50%Pd/Au have been calculated for comparison. At a surface coverage of 1/2 ML, CO starts to adsorb at the Pd/Au interfacial site. The free adsorption energy of CO is calculated using Equations 2, S6, and S17.

investigated the adsorption of *CO on atop sites at different CO surface coverages (Figure 5). Similar conclusions were obtained that the adsorption energy of *CO at the interfacial sites of the Pd/Au(111) surface is weaker than that over the pure Pd(111) surface at various *CO surface coverages. Thus, the *CO adsorption site will not change our conclusion that a high surface coverage of *CO can promote the exposure of the bimetallic interface sites.

Selectivity of long-chain C_{3+} chemicals vs. methane

To enhance the selectivity of CO_2RR-to-C_{3+}, one needs to promote the *CH_2–C_1 coupling (the potential RDS for CO_2RR-to-C_{3+}) and suppress the CH_2 further reduction to methane (CH_4). The free energy diagram shows that CH_2-to-CH_4 is very exothermic (Figures S40 and S41). We then examined the activation barrier for the CH_2–C_1 coupling and reduction of *CH_2 to CH_4 to investigate the selectivity of forming C_{3+} vs. CH_4 over the Pd/Au catalysts.

At a low *CO coverage (i.e., 1/16 ML), all examined sites (e.g., Pd(111), Pd sites of Pd/Au(111), and the interface sites of Pd/Au(111)) show higher activation barriers for the formation of CH_4 than that of *CH_2–C_1 coupling (Figures 6 and S42–S46). In particular for the interface site of the Pd/Au(111) surface, the activation barriers of all the examined reactions are lower than those over the Pd sites of Pd/Au(111) and Pd(111). As for the methane formation over the interface site of Pd/Au(111), *CH can be easily reduced to *CH_2 with a low activation barrier of 1.00 eV. Then, the activation barrier for the next step to *CH_3 slightly increases by 0.29 eV. However, the activation barrier from *CH_3 to methane is significantly high, on the order of 1.94 eV. This is 0.6 eV higher than that of the *CH_2–COH coupling (the potential RDS for CO_2RR-to-C_{3+}). The higher activation barrier comes from the CH_3 reduction step than other CH_2 reduction steps over the Pd/Au alloy system is that (1) the transition state configurations are initial state-like ones (Figures S43 and S44) and (2) in the case of the *CH_2 reduction to *CH_3, it only involves the *CH_2 migration over the PdAu(111) surface, while for the *CH_3 reduction to methane step, it involves both the migration of *CH_3 and *H migration in the transition states. According to the activation barrier comparison,

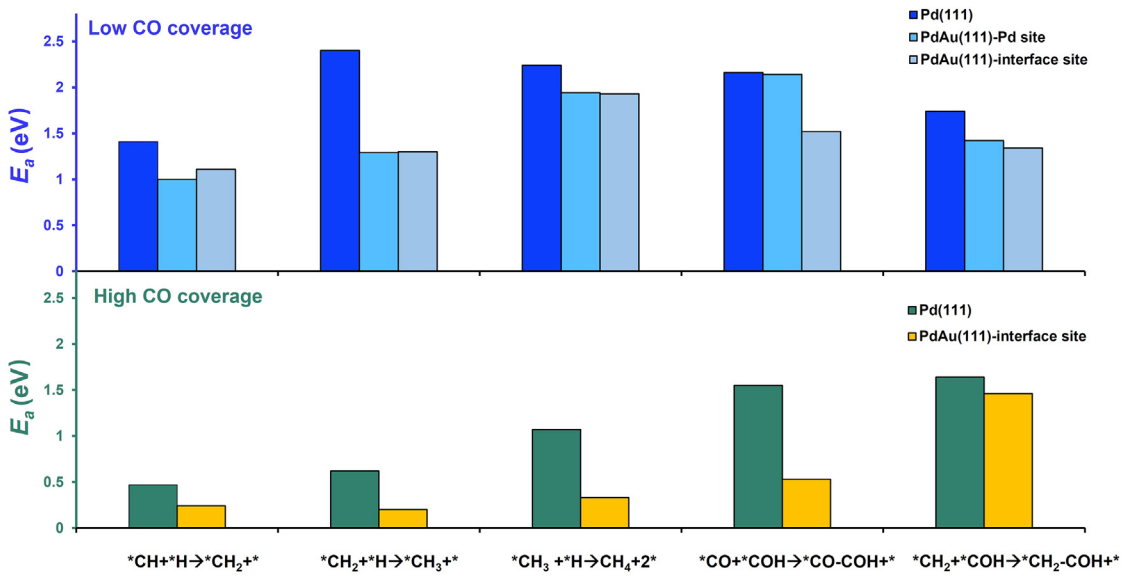

Figure 6. Selectivity of methane formation vs. C–C coupling

We compare the activation barriers between methane formation and C–C coupling processes over the Pd(111) and Pd/Au(111) surfaces at low (i.e., 1/16 ML) and high (i.e., 1/2 ML) *CO coverage. For the Pd/Au(111) surface, we have examined both the pure Pd site and the Pd/Au interface site at a low *CO coverage. For the high *CO coverage, the intermediates adsorb at the Pd/Au interface sites.

CO_2RR-to-methane over the Pd/Au(111) surface is kinetically difficult to occur due to the high activation barrier of methane formation from *CH_3. The intermediate *CH_2 will participate during the *CH_2–C_1 coupling process to generate C_{3+} long chain hydrocarbons during the CO_2RR process.

At a high CO coverage (i.e., 1/2 ML), the activation barriers of all examined reactions decreased significantly (Figures 6 and S47–S51). Taking *CH_2–COH as an example, its activation barrier over the Pd/Au interface site decreased from 1.34 eV to 0.53 eV. The reason is that a high *CO coverage weakened the *CO (or *COH or *CH_2) binding strength over the Pd/Au(111) surface (Figure 5) and thus, *CO (or *COH or *CH_2) would be more easier to diffuse over the surface and facilitate C_1–C_1 coupling processes.[63] At elevated *CO coverage levels, the reduction to methane pathway originating from *CH_2 species can become competitive with the C–C coupling reaction due to their closely matched activation barriers. However, the *H concentration over the surface can be limited due to the high surface coverage of *CO and thus, suppress the formation of methane.

Engineering the bimetallic interfaces via tuning the Pd/Au ratios

We have shown that the *CH_2–C_1 coupling could be the potential RDS step and *CH_2 could be the essential intermediate to determine the selectivity of CO_2RR-to-C_{3+}. To promote the C_{3+} formation from CO_2RR, one needs to lower the activation barriers of *CH_2–C_1 coupling. Based on our DFT results for the adsorption energy comparison between *CH_2 and *COH along with the activation barrier, activation barriers of *CH_2–C_1 coupling are closely correlated with the adsorption energy of *CH_2 (Figure S52). Thus, one strategy to lower the activation barrier of the *CH_2–C_1 coupling is to optimize the binding strength of key intermediate *CH_2 via tuning the Pd/Au ratios.

We then examined the *CH_2 adsorption and *COH–CH_2 coupling over various Pd/Au(111) alloy surfaces, including bare Pd, 87.5%Pd/Au, 75% Pd/Au, 62.5% Pd/Au,

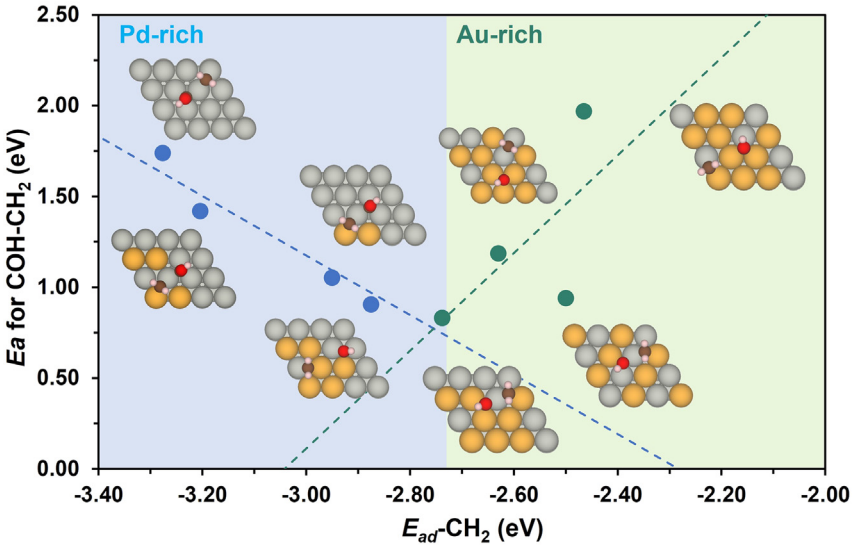

Figure 7. A volcano correlation between the C–C coupling and the CH2 adsorption

We correlate activation energy (E_a) of *CH_2–C_1 coupling (the potential RDS of CO_2RR-to-C_{3+}) and the *CH_2 adsorption energy (E_{ad}–CH_2) at the Pd/Au interface site with different Au/Pd ratios.

50% Pd/Au, 43.75% Pd/Au, and 37.5% Pd/Au (Figures S53 and S54). Interestingly, our DFT results show a volcano relationship between the activation barrier for *COH–CH_2 coupling and the *CH_2 adsorption energy (Figure 7). As depicted in Figure 7, it is evident that the activation barrier for CH_2–C_1 coupling reactions exhibits a decrease as more Au atoms are doped within the surface. However, once the ratio between Pd and Au reaches 1, the trend reverses, and the activation barrier starts to increase. The observed phenomenon can be explained by considering the diffusion of adsorbates from the initial state to the transition state. In the region where the Pd/Au ratio ranges from 62.5% to 50% (as depicted in Figures S54C–S54E), a lower activation barrier is observed. This is attributed to the migration of *CH_2 from interface sites to Pd sites in the transition states. Such diffusion to the more stable Pd sites significantly reduces the activation barrier for C–C coupling reactions. Conversely, in cases where *CH_2 migrates from interface sites to Au sites (as shown in Figure S54G), the resulting transition states are unstable, leading to higher activation barriers. In Figure S54A and S54F, *CH_2 is observed to diffuse from Pd bridge sites to the Pd top sites. The activation barrier for this process is relatively higher due to the strong binding strength of *CH_2 in the initial states.

According to this volcano plot, the optimal bimetallic surface Pd/Au ratio of 1:1 was obtained with the minimum activation barrier of *CH_2–C_1 coupling of 0.83 eV and the corresponding *CH_2 binding energy of −2.74 eV. To gain insights into the selectivity, we have also investigated the HER on the 50%Pd/Au(111) surface (Figure S55). We found that the PdAu(111) interfacial site exhibits a notable suppression of HER when compared with the pure Pd surface or the Pd site of the PdAu alloy system.

d-Band center analysis

We further analyzed the electronic structures of the Pd/Au surface interface sites at different Au/Pd ratios. Finding the optimal electronic structures (e.g., *d*-band center[64,65]) of Pd/Au, which could lead to an optimal binding strength of intermediates *CH_2 on the catalyst surface, are crucial to promote the C_{3+} formation.

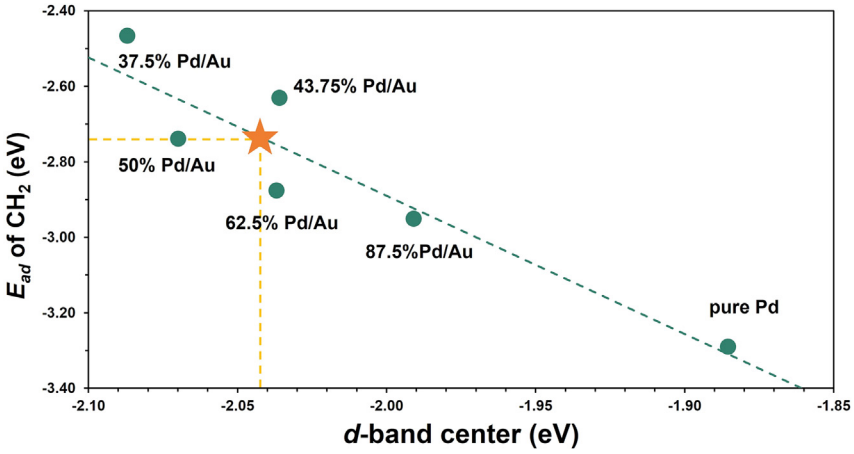

Figure 8. Optimal *d*-band center of Pd for C–C coupling over the interface site

A linear relationship between the key intermediate *CH_2 adsorption energy and the *d*-band center of various Pd/Au(111) bimetallic surfaces.

Our results show (Figure 8) that the adsorption of key intermediate *CH_2 over the Pd/Au interface site was linearly strengthened as decreasing the *d*-band center (note: the Pd *d*-band center of the *CH_2 adsorbed site). Our results correspond well with Hammer and Nørskov's *d*-band theory.[66] In general, a strong bond occurs if antibonding states are shifted up through the Fermi level (and become empty) and bonding states are shifted down through the Fermi level (and become filled). The bonding contribution stems from Pd atoms, whereas Au atoms predominantly contribute to the antibonding interactions. Therefore, we plotted the relationship between *CH_2 adsorption energy and the *d*-band center of the Pd atom located on the interface site in Figure 8 *d*-band center shifts away from Fermi level result in weaker adsorption energy of the adsorbates because a lower *d*-band center will make the antibonding states partially filled and lead to a weaker adsorption, and vice versa.[67] Therefore, our work suggests that the *d*-band center of the bimetallic interface could serve as a key descriptor to promote the C–C coupling and thus, enhance the selectivity of CO_2RR-to-C_{3+}. The optimal *d*-band center of the bimetallic interface site is −2.90 eV.

In this work, we have comprehensively explored the reaction mechanism of CO_2RR-to-C_{3+} over the Pd/Au bimetallic systems. Based on our DFT calculations, *CH_2–C_1 coupling step could be the RDS and *CH_2 could be the key intermediate over the bimetallic interface sites to generate long carbon chain C_{3+} chemicals. To enhance the selectivity of CO_2RR-to-C_{3+}, one strategy is to increase the *CO surface coverage to expose the Pd/Au interface site for the *CH_2–C_1 coupling. Another strategy is to tune the binding strength of the key intermediate *CH_2 via engineering the *d*-band center of the bimetallic interfacial Pd/Au site. Via tuning the Au/Pd ratios, a volcano correlation between the *CH_2 adsorption and the activation barrier of *CH_2–C_1 coupling was established. This leads to an optimal bimetallic surface ratio of Pd/Au (1/1) bimetallic catalyst with an optimal *d*-band center of around −2.90 eV. Our work provides the fundamental understandings of CO_2RR-to-C_{3+} reaction mechanisms and identifies the key descriptors of influencing the C_{3+} selectivity (*CO surface coverage and *d*-band center). Our work also creates a rational design of engineering bimetallic interfaces for generating value-added C_{3+} liquid chemicals from CO_2RR using renewable electricity.

EXPERIMENTAL PROCEDURES

Resource availability

Lead contact

Any requests for information can be directed to the lead contact, Fanglin Che (fanglin_che@uml.edu).

Materials availability

No materials were used for this study.

Data and code availability

The authors state that the data supporting the results of this study can be found within the paper and the Supplementary Information. Any additional data can be obtained by reaching out to the Lead Contact upon making a reasonable request.

SUPPLEMENTAL INFORMATION

Supplemental information can be found online at https://doi.org/10.1016/j.xcrp.2023.101718.

ACKNOWLEDGMENTS

Y.X., M.B.R., and F.C. thank the sponsorship by Department of Navy award N00014-22-1-2001 issued by the Office of Naval Research. The United States Government has a royalty-free license throughout the world in all copyrightable material contained herein. F.C. also thanks the support provided by Department of Energy, Basic Energy Science, Catalysis Science, Early Career Research Program under the award number of DE-SC0024553. H.X. acknowledges the support from the NSF Chemical Catalysis Program (CHE-2102363). Y.X. and F.C. also acknowledge the computational resources provided by the Massachusetts Green High-Performance Computing Center (MGHPCC). This work used the San Diego Supercomputer Center at University of California San Diego through allocation No. CHM220016, No. CHE200083, and No. CHE220075 from the Advanced Cyberinfrastructure Coordination Ecosystem: Services & Support (ACCESS) program, which is supported by National Science Foundation grants #2103478.[36]

AUTHOR CONTRIBUTIONS

F.C. designed the research and supervised the project; Y.X. carried out the project calculations, data analysis, and wrote the paper; Y.X., M.B.R., H.X., and F.C. discussed the results and contributed to the preparation of the manuscript.

DECLARATION OF INTERESTS

The authors declare no competing interests.

INCLUSION AND DIVERSITY

One or more of the authors of this paper self-identifies as a gender minority in their field of research.

Received: July 29, 2023
Revised: October 5, 2023
Accepted: November 9, 2023
Published: December 1, 2023

REFERENCES

1. Marques Mota, F., and Kim, D.H. (2019). From CO_2 methanation to ambitious long-chain hydrocarbons: alternative fuels paving the path to sustainability. Chem. Soc. Rev. *48*, 205–259.
2. Fazlollahi, F., Bown, A., Ebrahimzadeh, E., and Baxter, L.L. (2015). Design and analysis of the natural gas liquefaction optimization process-CCC-ES (energy storage of cryogenic carbon capture). Energy *90*, 244–257.
3. Ross, M.B., De Luna, P., Li, Y., Dinh, C.-T., Kim, D., Yang, P., and Sargent, E.H. (2019). Designing materials for electrochemical carbon dioxide recycling. Nat. Catal. *2*, 648–658.
4. Cordon, M.J., Zhang, J., Purdy, S.C., Wegener, E.C., Unocic, K.A., Allard, L.F., Zhou, M., Assary, R.S., Miller, J.T., Krause, T.R., et al. (2021). Selective butene formation in direct ethanol-to-C_{3+}-olefin valorization over Zn–Y/Beta and single-atom alloy composite catalysts using In Situ-generated hydrogen. ACS Catal. *11*, 7193–7209.
5. Zhou, H., Wang, B., Wang, F., Yu, X., Ma, L., Li, A., and Reetz, M.T. (2019). Chemo-and regioselective dihydroxylation of benzene to hydroquinone enabled by engineered cytochrome P450 monooxygenase. Angew. Chem., Int. Ed. Engl. *131*, 774–778.
6. Besson, M., Gallezot, P., and Pinel, C. (2014). Conversion of biomass into chemicals over metal catalysts. Chem. Rev. *114*, 1827–1870.
7. De Luna, P., Hahn, C., Higgins, D., Jaffer, S.A., Jaramillo, T.F., and Sargent, E.H. (2019). What would it take for renewably powered electrosynthesis to displace petrochemical processes? Science *364*, eaav3506.
8. Savilov, S., Suslova, E., Epishev, V., Tveritinova, E., Zhitnev, Y., Ulyanov, A., Maslakov, K., and Isaikina, O. (2021). Conversion of secondary C_3-C_4 aliphatic alcohols on carbon nanotubes consolidated by spark plasma sintering. Nanomaterials *11*, 352.
9. Bushuyev, O.S., De Luna, P., Dinh, C.T., Tao, L., Saur, G., van de Lagemaat, J., Kelley, S.O., and Sargent, E.H. (2018). What should we make with CO_2 and how can we make it? Joule *2*, 825–832.
10. Wu, J., Ma, S., Sun, J., Gold, J.I., Tiwary, C., Kim, B., Zhu, L., Chopra, N., Odeh, I.N., Vajtai, R., et al. (2016). A metal-free electrocatalyst for carbon dioxide reduction to multi-carbon hydrocarbons and oxygenates. Nat. Commun. *7*, 13869.
11. Lee, S., Kim, D., and Lee, J. (2015). Electrocatalytic production of C_3-C_4 compounds by conversion of CO_2 on a chloride-induced Bi-phasic Cu_2O-Cu catalyst. Angew. Chem., Int. Ed. Engl. *127*, 14914–14918.
12. Masa, J., Andronescu, C., and Schuhmann, W. (2020). Electrocatalysis as the nexus for sustainable renewable energy: the gordian knot of activity, stability, and selectivity. Angew. Chem., Int. Ed. Engl. *59*, 15298–15312.
13. Kim, T., Kargar, A., Luo, Y., Mohammed, R., Martinez-Loran, E., Ganapathi, A., Shah, P., and Fenning, D.P. (2018). Enhancing C_2–C_3 production from CO_2 on copper electrocatalysts via a potential-dependent mesostructure. ACS A.E.M. *1*, 1965–1972.
14. Zhu, D.D., Liu, J.L., and Qiao, S.Z. (2016). Recent advances in inorganic heterogeneous electrocatalysts for reduction of carbon dioxide. Adv. Mater. *28*, 3423–3452.
15. Cao, C., Ma, D.D., Jia, J., Xu, Q., Wu, X.T., and Zhu, Q.L. (2021). Divergent Paths, Same Goal: A Pair-Electrosynthesis tactic for cost-efficient and exclusive formate production by metal–organic-framework-derived 2D electrocatalysts. Adv. Mater. *33*, 2008631.
16. Jaster, T., Gawel, A., Siegmund, D., Holzmann, J., Lohmann, H., Klemm, E., and Apfel, U.-P. (2022). Electrochemical CO_2 reduction toward multicarbon alcohols - the microscopic world of catalysts & process conditions. iScience *25*, 104010.
17. Zhou, Y., Martín, A.J., Dattila, F., Xi, S., López, N., Pérez-Ramírez, J., and Yeo, B.S. (2022). Long-chain hydrocarbons by CO_2 electroreduction using polarized nickel catalysts. Nat. Catal. *5*, 545–554.
18. Maeng, J.Y., Hwang, S.Y., Kim, Y.J., Yoon, I., Myung, C.W., Rhee, C.K., and Sohn, Y. (2023). Electrochemical CO_2/CO reduction and C–C coupling path for mimicking Fischer–Tropsch synthesis over cadmium electrodes. J. Phys. Chem. C *127*, 11448–11461.
19. Chang, C.-C., Ku, M.-S., Lien, W.-H., and Hung, S.-F. (2022). Unveiling the bonding nature of C_3 intermediates in the CO_2 reduction reaction through the oxygen-deficient Cu_2O(110) surface–a DFT Study. J. Phys. Chem. C *126*, 5502–5512.
20. Peng, C., Luo, G., Zhang, J., Chen, M., Wang, Z., Sham, T.-K., Zhang, L., Li, Y., and Zheng, G. (2021). Double sulfur vacancies by lithium tuning enhance CO_2 electroreduction to n-propanol. Nat. Commun. *12*, 1580.
21. Peterson, A.A., and Nørskov, J.K. (2012). Activity descriptors for CO_2 electroreduction to methane on transition-metal catalysts. J. Phys. Chem. Lett. *3*, 251–258.
22. Hori, Y., Murata, A., Tsukamoto, T., Wakebe, H., Koga, O., and Yamazaki, H. (1994). Adsoprtion of carbon monoxide at a copper electrode accompanied by electron transfer observed by voltammetry and IR spectroscopy. Electrochim. Acta *39*, 2495–2500.
23. Zhao, Q., Martirez, J.M.P., and Carter, E.A. (2022). Charting C–C coupling pathways in electrochemical CO_2 reduction on Cu (111) using embedded correlated wavefunction theory. Proc. Natl. Acad. Sci. USA *119*. e2202931119.
24. Zhou, Y., Che, F., Liu, M., Zou, C., Liang, Z., De Luna, P., Yuan, H., Li, J., Wang, Z., Xie, H., et al. (2018). Dopant-induced electron localization drives CO_2 reduction to C_2 hydrocarbons. Nat. Chem. *10*, 974–980.
25. Xiao, H., Goddard, W.A., III, Cheng, T., and Liu, Y. (2017). Cu metal embedded in oxidized matrix catalyst to promote CO_2 activation and CO dimerization for electrochemical reduction of CO_2. Proc. Natl. Acad. Sci. USA *114*, 6685–6688.
26. Zhu, W., Michalsky, R., Metin, Ö., Lv, H., Guo, S., Wright, C.J., Sun, X., Peterson, A.A., and Sun, S. (2013). Monodisperse Au nanoparticles for selective electrocatalytic reduction of CO_2 to CO. J. Appl. Comput. Sci. *135*, 16833–16836.
27. Rosen, J., Hutchings, G.S., Lu, Q., Rivera, S., Zhou, Y., Vlachos, D.G., and Jiao, F. (2015). Mechanistic insights into the electrochemical reduction of CO_2 to CO on nanostructured Ag surfaces. ACS Catal. *5*, 4293–4299.
28. Chen, M., Wu, B., Yang, J., and Zheng, N. (2012). Small adsorbate-assisted shape control of Pd and Pt nanocrystals. Adv. Mater. *24*, 862–879.
29. Gao, D., Zhou, H., Wang, J., Miao, S., Yang, F., Wang, G., Wang, J., and Bao, X. (2015). Size-dependent electrocatalytic reduction of CO_2 over Pd nanoparticles. J. Appl. Comput. Sci. *137*, 4288–4291.
30. Lum, Y., Huang, J.E., Wang, Z., Luo, M., Nam, D.-H., Leow, W.R., Chen, B., Wicks, J., Li, Y.C., Wang, Y., et al. (2020). Tuning OH binding energy enables selective electrochemical oxidation of ethylene to ethylene glycol. Nat. Catal. *3*, 14–22.
31. Feng, Y., Yang, H., Zhang, Y., Huang, X., Li, L., Cheng, T., and Shao, Q. (2020). Te-doped Pd nanocrystal for electrochemical urea production by efficiently coupling carbon dioxide reduction with nitrite reduction. Nano Lett. *20*, 8282–8289.
32. Kortlever, R., Peters, I., Balemans, C., Kas, R., Kwon, Y., Mul, G., and Koper, M.T.M. (2016). Palladium–gold catalyst for the electrochemical reduction of CO_2 to C_1–C_5 hydrocarbons. Chem. Commun. *52*, 10229–10232.
33. Dong, X., Li, J., Ma, T., and Wang, L. (2022). Insights into the mechanism of carbon chain growth on zeolite-based Fischer–Tropsch Co/Y catalysts. Phys. Chem. Chem. Phys. *24*, 14751–14762.
34. Chen, Q., Tsiakaras, P., and Shen, P. (2022). Electrochemical reduction of carbon dioxide: recent advances on Au-based nanocatalysts. Catalyst *12*, 1348.
35. Rahaman, M., Kiran, K., Montiel, I.Z., Grozovski, V., Dutta, A., and Broekmann, P. (2020). Selective n-propanol formation from CO_2 over degradation-resistant activated PdCu alloy foam electrocatalysts. Green Chem. *22*, 6497–6509.
36. Boerner, T.J., Deems, S., Furlani, T.R., Knuth, S.L., and Towns, J. (2023). ACCESS: advancing innovation: NSF's advanced cyberinfrastructure coordination ecosystem: services & support. Practice and Experience in Advanced Research Computing. Association for Computing Machinery.
37. Grabow, L.C., and Mavrikakis, M. (2011). Mechanism of methanol synthesis on Cu through CO_2 and CO hydrogenation. ACS Catal. *1*, 365–384.
38. Ou, L. (2015). Chemical and electrochemical hydrogenation of CO_2 to hydrocarbons on Cu

single crystal surfaces: insights into the mechanism and selectivity from DFT calculations. RSC Adv. *5*, 57361–57371.

39. Wang, X., Wang, Z., Zhuang, T.-T., Dinh, C.-T., Li, J., Nam, D.-H., Li, F., Huang, C.-W., Tan, C.-S., Chen, Z., et al. (2019). Efficient upgrading of CO to C_3 fuel using asymmetric C-C coupling active sites. Nat. Commun. *10*, 5186.

40. Kresse, G., and Hafner, J. (1993). Ab initio molecular dynamics for liquid metals. Phys. Rev. B Condens. Matter *47*, 558–561.

41. Zhang, Y., and Yang, W. (1998). Comment on "Generalized gradient approximation made simple". PRL *80*, 890.

42. Gao, D., Zhou, H., Cai, F., Wang, J., Wang, G., and Bao, X. (2018). Pd-containing nanostructures for electrochemical CO_2 reduction reaction. ACS Catal. *8*, 1510–1519.

43. Saavedra, J., Doan, H.A., Pursell, C.J., Grabow, L.C., and Chandler, B.D. (2014). The critical role of water at the gold-titania interface in catalytic CO oxidation. Science *345*, 1599–1602.

44. Pillai, H.S., and Xin, H. (2019). New insights into electrochemical ammonia oxidation on Pt (100) from first principles. Ind. Eng. Chem. Res. *58*, 10819–10828.

45. Mathew, K., Kolluru, V.S.C., Mula, S., Steinmann, S.N., and Hennig, R.G. (2019). Implicit self-consistent electrolyte model in plane-wave density-functional theory. J. Chem. Phys. *151*, 234101.

46. Petrosyan, S.A., Rigos, A.A., and Arias, T.A. (2005). Joint density-functional theory: Ab Initio study of Cr_2O_3 surface chemistry in solution. J. Phys. Chem. B *109*, 15436–15444.

47. Mathew, K., Sundararaman, R., Letchworth-Weaver, K., Arias, T.A., and Hennig, R.G. (2014). Implicit solvation model for density-functional study of nanocrystal surfaces and reaction pathways. J. Chem. Phys. *140*, 084106.

48. Goodpaster, J.D., Bell, A.T., and Head-Gordon, M. (2016). Identification of possible pathways for C–C bond formation during electrochemical reduction of CO_2: new theoretical insights from an improved electrochemical model. J. Phys. Chem. Lett. *7*, 1471–1477.

49. Hörmann, N.G., Andreussi, O., and Marzari, N. (2019). Grand canonical simulations of electrochemical interfaces in implicit solvation models. J. Chem. Phys. *150*, 041730.

50. Steinmann, S.N., and Sautet, P. (2016). Assessing a first-principles model of an electrochemical interface by comparison with experiment. J. Phys. Chem. C *120*, 5619–5623.

51. Garza, A.J., Bell, A.T., and Head-Gordon, M. (2018). Mechanism of CO_2 Reduction at copper surfaces: pathways to C_2 products. ACS Catal. *8*, 1490–1499.

52. Mu, Z., Han, N., Xu, D., Tian, B., Wang, F., Wang, Y., Sun, Y., Liu, C., Zhang, P., Wu, X., et al. (2022). Critical role of hydrogen sorption kinetics in electrocatalytic CO_2 reduction revealed by on-chip in situ transport investigations. Nat. Commun. *13*, 6911.

53. Jinnouchi, R., and Anderson, A.B. (2008). Aqueous and surface redox potentials from self-consistently determined Gibbs energies. J. Phys. Chem. C *112*, 8747–8750.

54. Jinnouchi, R., and Anderson, A.B. (2008). Electronic structure calculations of liquid-solid interfaces: Combination of density functional theory and modified Poisson-Boltzmann theory. Phys. Rev. B *77*, 245417.

55. Xiao, H., Cheng, T., and Goddard, W.A., III (2017). Atomistic mechanisms underlying selectivities in C_1 and C_2 products from electrochemical reduction of CO on Cu(111). J. Appl. Comput. Sci. *139*, 130–136.

56. Foppa, L., Iannuzzi, M., Copéret, C., and Comas-Vives, A. (2019). Facile Fischer–Tropsch Chain Growth from CH_2 monomers enabled by the dynamic CO adlayer. ACS Catal. *9*, 6571–6582.

57. Lu, J.-N., Liu, J., Zhang, L., Dong, L.-Z., Li, S.-L., and Lan, Y.-Q. (2021). Crystalline mixed-valence copper supramolecular isomers for electroreduction of CO_2 to hydrocarbons. J. Mater. Chem. A *9*, 23477–23484.

58. Huang, M., Gong, S., Wang, C., Yang, Y., Jiang, P., Wang, P., Hu, L., and Chen, Q. (2021). Lewis-basic EDTA as a highly active molecular electrocatalyst for CO_2 reduction to CH_4. Angew. Chem., Int. Ed. Engl. *60*, 23002–23009.

59. Hossain, M.D., Huang, Y., Yu, T.H., Goddard, W.A., Iii, and Luo, Z. (2020). Reaction mechanism and kinetics for CO_2 reduction on nickel single atom catalysts from quantum mechanics. Nat. Commun. *11*, 2256.

60. Singh, M.R., Goodpaster, J.D., Weber, A.Z., Head-Gordon, M., and Bell, A.T. (2017). Mechanistic insights into electrochemical reduction of CO_2 over Ag using DFT and transport models. Proc. Natl. Acad. Sci. USA *114*, E8812–E8821.

61. Zeinalipour-Yazdi, C.D., Willock, D.J., Thomas, L., Wilson, K., and Lee, A.F. (2016). CO adsorption over Pd nanoparticles: a general framework for IR simulations on nanoparticles. Surf. Sci. *646*, 210–220.

62. Köhler, L., and Kresse, G. (2004). Density functional study of CO on Rh (111). Phys. Rev. B *70*, 165405.

63. Huang, Y., Handoko, A.D., Hirunsit, P., and Yeo, B.S. (2017). Electrochemical reduction of CO_2 using copper single-crystal surfaces: effects of CO* coverage on the selective formation of ethylene. ACS Catal. *7*, 1749–1756.

64. Jiao, S., Fu, X., and Huang, H. (2022). Descriptors for the evaluation of electrocatalytic reactions: d-band theory and beyond. Adv. Funct. Mater. *32*, 2107651.

65. Ouyang, M., Papanikolaou, K.G., Boubnov, A., Hoffman, A.S., Giannakakis, G., Bare, S.R., Stamatakis, M., Flytzani-Stephanopoulos, M., and Sykes, E.C.H. (2021). Directing reaction pathways via in situ control of active site geometries in PdAu single-atom alloy catalysts. Nat. Commun. *12*, 1549.

66. Hammer, B., and Norskov, J.K. (1995). Why gold is the noblest of all the metals. Nature *376*, 238–240.

67. Wang, Z., Huang, J., Wang, L., Liu, Y., Liu, W., Zhao, S., and Liu, Z.Q. (2022). Cation-tuning induced d-band center modulation on Co-based spinel oxide for oxygen reduction/evolution reaction. Angew. Chem., Int. Ed. Engl. *61*, e202114696.